Optics Letters

Three-dimensional location system based on an L-shaped array of Rydberg atomic receivers

Yang Yan,[1,2] Jinpeng Yuan,[1,2,3] Linjie Zhang,[1,2] Liantuan Xiao,[1,2] Suotang Jia,[1,2] and Lirong Wang[1,2,*]

[1]State Key Laboratory of Quantum Optics and Quantum Optics Devices, Institute of Laser Spectroscopy, Shanxi University, 92 Wucheng Road, Taiyuan 030006, China
[2]Collaborative Innovation Center of Extreme Optics, Shanxi University, 92 Wucheng Road, Taiyuan 030006, China
[3]yjp@sxu.edu.cn
*wlr@sxu.edu.cn

Received 22 May 2023; revised 29 June 2023; accepted 4 July 2023; posted 5 July 2023; published 20 July 2023

The Rydberg atomic receiver, sensing microwave electric field with high sensitivity and broad bandwidth, possesses the potential to be the staple for precise navigation and remote sensing. In this Letter, a Ku-band three-dimensional location system using an L-shaped array of Rydberg atomic receivers is theoretically proposed and experimentally demonstrated, and the proof of principle results show excellent consistency between the location-derived and the setting coordinates. The novel L-shaped array, together with the triangulation method, gives both phase difference and angle of arrival, achieving location of the horn for a signal microwave field in three-dimensional space. The concluded validity of this location system in the testing scene remains at approximately 90% with a theoretical maximum location tolerance of 5.7 mm. Furthermore, the estimation of two different spatiotemporal coordinates for the moving target confirms the velocity measurement capability of the system with errors less than 0.5 mm/s. The proposed location system using a Rydberg atomic receiver array is a verification for the most basic element and can be extended through repetition or nesting to a multi-input–multi-output system as well as multi-channel information processing.

https://doi.org/10.1364/OL.496057

The accurate location estimation of a radiation source in three-dimensional (3D) space depends on the detector with excellent performance in signal collection, sorting, and recognition, promising in areas like wireless communication, target tracking, navigation, and positioning [1,2]. Different from the traditional echo-detection type location method, a passive location protocol not only determines the target location by sensing electromagnetic wave signals radiated from radiation sources, but also radiates no electromagnetic waves actively, which avoids exposing its own location [3,4]. Furthermore, assembling the detectors into an array with a programmable geometric configuration, which provides the ability of inherent correlation and multi-channel information capture capability, provides a new dimension of observation under passive location protocol combined with the triangulation method [5–7]. With the gradual development of the passive location protocol, several location methods based on specific parameters, such as time difference of arrival (TDOA), received signal strength (RSS), phase difference of arrival (PDOA), as well as angle of arrival (AOA), have been derived [8–13].

The Rydberg atom-based microwave electromagnetic field (MW E-field) receivers have potential in detector elements for locating, because of their outstanding characteristics such as high sensitivity, broad bandwidth, SI-traceability, stealth, and integration [14–17]. The optical readout methods, based on electromagnetically induced transparency (EIT) and Autler–Townes splitting (ATS) mechanisms, and the introduction of concurrent technology push the boundary of the sensitivity [18–22]. Especially, the Rydberg atomic superheterodyne receiver not only brings a new sensitivity millstone for a single detector element but also provides the ability for phase sensing, which establishes a foundation for spatial location estimation and phase encoding [23]. Heterodyne, modulation, internal state interference, and other means have also been introduced into this scheme to improve the phase-sensing accuracy [24–30]. Note that the geometry of the receivers is highly correlated with the array's perceived dimension of location, and a two-point linear array is recently used in AOA measurement [31,32]. However, the location in 3D space using the Rydberg atomic receiver, which, in more general demands, is still a task urgently needing to be solved.

In this Letter, an L-shaped array of Rydberg atomic receivers with adjustable capacity is constructed in two orthogonal planes. An algorithm combining the triangulation method with the joint PDOA and AOA estimation is proposed theoretically and demonstrated experimentally. The validity of the location system with theoretical maximum tolerance is verified and the potential source of error is evaluated. Afterward, two sets of spatiotemporal coordinates of the moving object are employed for velocity estimation. This work as a primary verification, based on one of the most basic array elements, can achieve higher precision spatiotemporal location and real-time velocity or pose response by replication, amplification, and nesting of the system.

The relevant atomic energy levels configuration employed in this experiment is shown in Fig. 1(a). A 780-nm weak probe field (red) drives the transition from the ground state $5S_{1/2}$ (F = 3) to

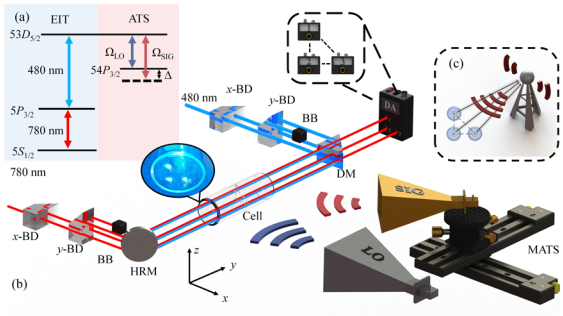

Fig. 1. (a) Relevant energy levels of the heterodyne configuration of Rb atoms. (b) Sketch of the experimental setup. BD, beam displacers; HRM, high-reflection mirror; Cell, Rb vapor cell; DM, dichroic mirror; BB, beam block; DA, detector array; MATS, multi-axial translation system. (c) Schematic diagram for realizing location based on an L-shaped array of Rydberg atomic receivers in 3D space. Inset is a photograph showing the generated L-shaped array.

the excited state $5P_{3/2}$ ($F' = 4$), and a 480-nm strong coupling field (blue) couples the excited state $5P_{3/2}$ ($F' = 4$) to the Rydberg state $53D_{5/2}$. Then the ladder-type three-level EIT is dressed by local oscillator (LO) and signal (SIG) MW fields, which drives the adjacent Rydberg transition of $53D_{5/2}$–$54P_{3/2}$. Figure 1(b) is the experimental setup for implementing the L-shaped array of Rydberg atomic receivers. The probe laser is provided by an external cavity diode laser (DL pro, Toptica), and its frequency is kept locked using saturation absorption spectroscopy method. The coupling laser, provided by a frequency-doubled amplified diode laser (TA-SHG pro, Toptica), maintains frequency locking by an additional EIT spectrum, which is not shown in Fig. 1. The powers of the probe and coupling lasers are 100 μW and 120 mW with beam diameters of 100 μm and 150 μm in the rubidium vapor cell, respectively. The corresponding Rabi frequencies are $33.6 \times 2\pi$ MHz and $18.0 \times 2\pi$ MHz. To construct the L-shaped array, the main probe beam is separated into four identical sub-beams, kept parallel spatially through a pair of specially designed orthogonal beam displacers (BDs). One of the sub-beams is obstructed by a beam block (BB). The separations between the two nearest sub-beams (baselines) are determined by the specification of the BD. In a similar way, the main coupling laser forms a symmetric L-shaped array. The three coupling sub-beams are overlapped with corresponding counter-propagating probe ones in the vapor cell, constructing three sensing channels in an L-shape. The all-identical receivers together with the isotropy of the atomic medium guarantee the validity of the signal. The amplitude difference among three detectors has no effect to the readout of the phase information. The inset indicates a photograph that shows the generated L-shaped array of coupling sub-beams inside the vapor cell. After leaving the vapor cell, probe sub-beams are filtered by a dichroic mirror (DM), collected by a detector array (DA), and shown on an oscilloscope. Note that the manufacturing tolerance of BDs determines the array's baseline error and then leads to mislocation. A CMOS camera is used to make a calibration about the grids of the array, so that a corrected baseline length of 9.8 mm is obtained and used in our theoretical analysis.

Two vector signal generators (SMB100 A, Rohde & Schwarz) are time synchronized to provide LO and SIG MW fields with a unified initial phase, which are emitted by two standard gain horn

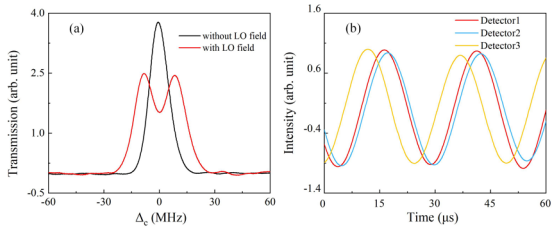

Fig. 2. (a) Transmission spectrum with/without the LO MW field recorded by detector 1. (b) Beat notes in three sensing channels.

antennas, respectively (referred as Horn LO and Horn SIG). A 14.232-GHz MW field serves as the LO field and the frequency of SIG MW field is 14.232 GHz + 23 kHz, where 23 kHz is defined as inter-frequency (IF). The position of Horn LO is fixed as a phase reference, and the Horn SIG shows high mobility with a multi-axial translation system (MATS), which consists of two programmable long-travel linear translation stages and a vertical translation stage. Both of the antennas are placed over 30 cm away from the cell to be in the far-field regime. All the lasers and MW fields are adjusted to vertical linear polarization to obtain the optimal signals. The input power of the LO field is −15 dBm and the input power of SIG field is −25 dBm, which are chosen such that the beat notes reflected in the probe lasers have the largest amplitudes [23]. Figure 1(c) schematically illustrates the location scheme for the SIG MW field in the proposed system. Three independent Rydberg atomic receivers arranged in an L-shape perceive the SIG field separately, such that the location information of the SIG field can be obtained from the array's inherent geometry relevance. Triggering the oscilloscope through the mixer signal also ensures synchronization among the receivers.

Figure 2(a) shows the spectrum used to obtain the original phase under the EIT-ATS scheme. A typical EIT spectrum [black line in Fig. 2(a)] occurs when the counter-propagated probe and coupling lasers are applied to atoms. Then, when the LO MW field is introduced, the Rydberg atomic receiver responds with an ATS spectrum [red line in Fig. 2(a)]. The SIG MW field with detuned frequency represents the target object to be detected. The two MW fields interfere and the resulting time-varying signal is called a beat note, which can be expressed as

$$E_{beat} = \sqrt{[E_{LO}\cos(\omega_{LO}t + \phi_{LO}) + E_{SIG}\cos(\omega_{SIG}t + \phi_{SIG})]^2}, \quad (1)$$

where E_{LO}, ω_{LO}, and ϕ_{LO} are the amplitude, frequency, and phase for field LO; and E_{SIG}, ω_{SIG}, and ϕ_{SIG} are those for field SIG. The atoms response to this changing electric field magnitude can be readout through the amplitude of the probe laser's transmission at the resonant frequency. The direct current component of the detected field will be filtered in the readout process for simplification. Therefore, for three sensing channels, the actual readout results of the E-field felt by the atoms can be written as

$$E_{atoms} \propto E_{LO}E_{SIG}\cos(\omega_{IF}t + \Delta\phi_{i,j}). \quad (2)$$

The phase difference, $\Delta\phi_{i,j} = \phi_i - \phi_j, i, j = 1, 2, 3$, carries location information during the wave path based on the L-shaped geometry. Figure 2(b) presents the beat notes in three sensing channels obtained from independent detectors, showing distinct phase shifts as the difference in receivers' spatial position. The ϕ_i is determined by comparing the beat note read out by atoms with the mixed signal of the signal generators in

three co-related lock-in amplifiers (SR830, Stanford Research System). When the position of target radiation source (Horn SIG) is determined, the corresponding phase differences among each sensing channel is also obtained by comparing their phases. According to the geometry inside the array, three sets of two-dimensional angles of arrival (2D AOAs), consisting of azimuth and pitch angles, are derived as (θ, ϵ_z), (σ, ϵ_x), and (ρ, ϵ_y) for each projective plane (e.g., plane x–y, y–z. and z–x). A more detailed derivation of 2D AOAs is expressed in Supplement 1. A single angle of arrival defines a cone of possible directions to the receiver and the intersection between the cones is used for solving ambiguity. Combined with two measurements under different carrier waves, specific spatial coordinates can be derived through the following calculation:

$$(x-x_1)^2+(y-y_1)^2+(z-z_1)^2 = \frac{\sin^2\theta * y^2 + 2 * \sin\theta\cos\theta * y * z + \cos^2\theta * z^2}{\cos {\epsilon_x}^2}, \tag{3a}$$

$$(x-x_2)^2+(y-y_2)^2+(z-z_2)^2 = \frac{\sin^2\sigma * z^2 + 2 * \sin\sigma\cos\sigma * z * x + \cos^2\sigma * x^2}{\cos {\epsilon_y}^2}, \tag{3b}$$

$$(x-x_3)^2+(y-y_3)^2+(z-z_3)^2 = \frac{\sin^2\rho * x^2 + 2 * \sin\rho\cos\rho * x * y + \cos^2\rho * y^2}{\cos {\epsilon_z}^2}, \tag{3c}$$

$$\sqrt{x^2+y^2+z^2} = n_m * \lambda_m + \frac{\phi_m}{2\pi} * \lambda_m = n_n * \lambda_n + \frac{\phi_n}{2\pi} * \lambda_n, \tag{3d}$$

where n_m and n_n are integral period number estimations, ϕ_m and ϕ_n are independent phase measurement results under different carrier waves, and λ_m and λ_n present as their reduced wavelength. Therefore, the 3D space coordinates of the target radiation source are obtained. Before estimations, the linearity analysis along the three orthogonal axes is performed, as detailed in Supplement 1, and a linear response of location system proposed for the displacement from any direction is proven. On this basis, the location estimation is further implemented. Using MATS shown in Fig. 1(b), the target radiation source is moved with an axial step of 10 μm along an optional direction [vector coordinate (9, 1, 0.6) in this Letter]. For simplicity, the beginning position of MATS is taken as the origin of the coordinate system. Figure 3 shows an exhibition of measured location coordinates obtained in six sequential positions. The theoretical maximum tolerance, derived as 5.7 mm, gives a reference accuracy of the system and is shown in Fig. 3 as spheres for visual references. As the frequency increases from the C to Q band, the theoretical tolerance for detection also shows a finite rise. A detailed description of theoretical maximum tolerance is presented in Supplement 1. The location validity is defined as the proportion of the number of coordinates located inside the maximum tolerance to the total number. The estimation results all locate in the range from 86.7% to 96.7% and are concluded around 90%. A stable location system with higher accuracy and smaller fluctuations is established. Note that a nested combination of different baselines will further improve the location accuracy.

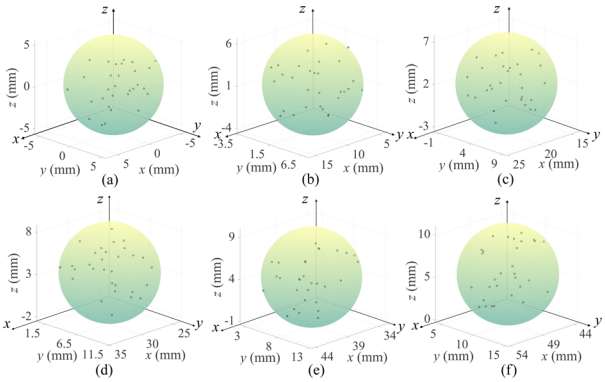

Fig. 3. Measured location coordinates (black circles) in 30 repetitions and the theoretical maximum tolerance (spheres) for visual reference. Panels (a)–(f) display six estimations in discrete positions.

The evaluation of the location system shows that the error source during estimation is mainly from three parts. The first is the influence of the background electromagnetic environment. An additional phase shift caused by scattering and multipath reflection comes from the apparatuses used in translocating the Horn SIG and pillaring the vapor cell in free space [18,33]. In addition to the existing quasi-anechoic room operating environment, a more accurate simulation of the electromagnetic environment will further correct the PDOA data. Furthermore, inside the vapor cell, the dielectric shell makes the RF fields standing waves, perturbing the phase of the field at a given location [34]. The second is errors from the device fabrication. The asymmetric supporting structures for the SIG and LO MW fields bring a misalignment. Although the incident SIG MW field radiated from the far-field regime can be seen as a plane wave, sidelobes will still have an effect on phase measurement. Relative polarization variation occurs during antenna movements and alignments. This effect makes amplitude changes only and causes no errors in PDOA sensing. The third is the inherent errors in array arrangement. For the same AOA, a location system with baseline shorter than half a wavelength results in a smaller phase shift compared with that with a longer baseline, which is harder to discern [35]. The effective diameter of the vapor cell limits the extension of the baseline. Large optical surfaces will enable more complex arrays to be realized, which is helpful for location with higher accuracy. Short interaction regions allow for clear origin identification of the coordinate system, which further improves the accuracy of location results. In addition, using multiple vapor cells to form nested arrays can improve this situation. Meanwhile, the phase resolution for a typical heterodyne Rydberg atomic mixer scheme is within 1° [23,26]. The phase error will lead to angle misestimation and further location misjudgment. Note that the introduction of magnetic field, amplitude modulation method, as well as an interferometry-like energy level structure will be options to improve the phase resolution [27,36,37].

Further, the velocity of the target radiation source is also derived, as shown in Fig. 4, using the estimated spatial coordinates and corresponding time information obtained during the measurement. The inset shows a sketch where the target radiation source moves with velocity v. On the way, three one-eighth concentric spheres are passed through where spatiotemporal coordinates are recorded. The MATS is electrically controlled so that the target radiation source keeps a uniform motion. A Doppler velocity spectrum is used as a reference as detailed in Supplement 1. A long-term measurement mode of the oscilloscope (RTO2000, Rohde & Schwarz) is used to record data and give timestamps. For every velocity in estimation, the results

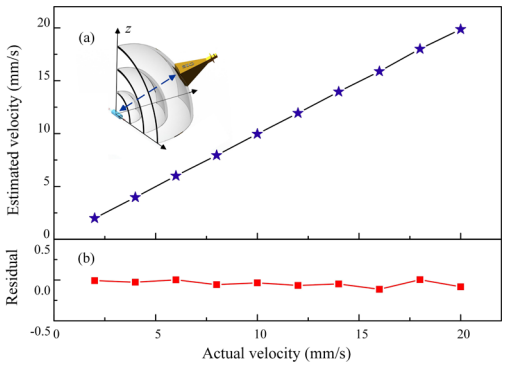

Fig. 4. (a) Estimation results for several set velocities of the target radiation source. (b) Corresponding residuals. Inset shows a sketch of the velocity measurement.

show good consistency with the actual values. The residuals are kept low as well as the maximum fluctuation is less than 0.5 mm/s during the whole process.

In conclusion, we have demonstrated a novel 3D location scheme based on an L-shaped array of Rydberg atomic receivers. An algorithm, combined the triangulation method with L-shaped geometry and joint PDOA and AOA estimation, is proposed. The proof of principle demonstration shows a concluded location validity of approximately 90% with a theoretical maximum tolerance of 5.7 mm. A velocity estimation for a moving target is obtained with errors less than 0.5 mm/s. As an element, an L-shaped array of Rydberg atomic receivers shows its potential for more complex array constructions.

In the demonstration, although the actual velocities are set low, our location system has a theoretical maximum detectable velocity of 21 mm/s with the concluded validity. The result comes from the 14.232-GHz carrier wave and 1-s time resolution. Adopting different carrier wavelength, increasing time resolution, developing the algorithm for integer ambiguity resolution, and the frequency-hopping pulse period perception technology are effective methods to adapt various requirements in velocity to be estimated. In the future, more elements laying in the array, more complex geometric arrangement, multi-array nesting, multi-parameter readout, and multi-target recognition will be the directions of publications.

Funding. National Natural Science Foundation of China (62075121); Fund Program for the Scientific Activities of Selected Returned Overseas Professionals in Shanxi Province (2023001); Shanxi "1331 Project".

Disclosures. The authors declare no conflicts of interest.

Data availability. Data underlying the results presented in this paper may be obtained from the authors upon reasonable request.

Supplemental document. See Supplement 1 for supporting content.

REFERENCES

1. R. Schmidt, IEEE Trans. Antennas Propag. **34**, 276 (1986).
2. F. Guo, Y. Fan, Y. Zhou, C. Zhou, and Q. Li, *Localization Principles in Space Electronic Reconnaissance* (National Defense Industry Press, 2012).
3. D. J. Torrieri, IEEE Trans. Aerosp. Electron. Syst. **AES-20**, 183 (1984).
4. D. Adamy, *EW 102: a Second Course in Electronic Warfare* (Artech House, 2004).
5. J. Yuan, H. Zhang, C. Wu, L. Wang, L. Xiao, and S. Jia, Opt. Lett. **46**, 4184 (2021).
6. L. Liu, Y. Zhang, Z. Li, R. Zhang, X. Yin, Y. Fei, L. Li, N. Liu, F. Xu, Y. Chen, and J. Pan, Nat. Photonics **15**, 137 (2021).
7. J. Yuan, H. Zhang, C. Wu, G. Chen, L. Wang, L. Xiao, and S. Jia, Laser Photonics Rev. **17**, 2200667 (2023).
8. M. M. Ahmed, K. C. Ho, and G. Wang, IEEE Trans. Signal Process. **68**, 4839 (2020).
9. A. Catovic and Z. Sahinoglu, IEEE Commun. Lett. **8**, 626 (2004).
10. K. C. Ho, IEEE Trans. Signal Process. **60**, 2101 (2012).
11. T. Lin, Z. Zhang, Y. Wang, Z. Zhu, S. Zhao, J. Liu, W. Jiang, and G. Wu, Opt. Express **28**, 38960 (2020).
12. A. Weiss, IEEE Signal Process. Lett. **11**, 513 (2004).
13. X. Wu, S. Gui, L. Zhou, Y. Wu, F. Yan, and Z. Tian, in *2022 IEEE 95th Vehicular Technology Conference: (VTC2022-Spring)* (2022), pp. 1–5.
14. J. A. Sedlacek, A. Schwettmann, H. Kübler, R. Löw, T. Pfau, and J. P. Shaffer, Nat. Phys. **8**, 819 (2012).
15. H. Q. Fan, S. Kumar, R. Daschner, H. Kübler, and J. P. Shaffer, Opt. Lett. **39**, 3030 (2014).
16. C. L. Holloway, J. A. Gordon, S. Jefferts, A. Schwarzkopf, D. A. Anderson, S. A. Miller, N. Thaicharoen, and G. Raithel, IEEE Trans. Antennas Propag. **62**, 6169 (2014).
17. S. Li, J. Yuan, L. Wang, L. Xiao, and S. Jia, Results Phys. **29**, 104728 (2021).
18. C. L. Holloway, M. T. Simons, J. A. Gordon, P. F. Wilson, C. M. Cooke, D. A. Anderson, and G. Raithel, IEEE Trans. Electromagn. Compat. **59**, 717 (2017).
19. S. Kumar, H. Fan, H. Kübler, J. Sheng, and J. P. Shaffer, Sci. Rep. **7**, 42981 (2017).
20. S. Li, J. Yuan, L. Wang, L. Xiao, and S. Jia, Front. Phys. **10**, 1 (2022).
21. Z. Liu, L. Zhang, B. Liu, Z. Zhang, G. Guo, D. Ding, and B. Shi, Nat. Commun. **13**, 1997 (2022).
22. M. Cai, S. You, S. Zhang, Z. Xu, and H. Liu, Appl. Phys. Lett. **122**, 161103 (2023).
23. M. Jing, Y. Hu, J. Ma, H. Zhang, L. Zhang, L. Xiao, and S. Jia, Nat. Phys. **16**, 911 (2020).
24. C. L. Holloway, M. T. Simons, J. A. Gordon, and D. Novotny, Antennas Wirel. Propag. Lett. **18**, 1853 (2019).
25. J. A. Gordon, M. T. Simons, A. H. Haddab, and C. L. Holloway, AIP Adv. **9**, 045030 (2019).
26. M. T. Simons, A. H. Haddab, J. A. Gordon, D. Novotny, and C. L. Holloway, IEEE Access **7**, 164975 (2019).
27. X.-B. Liu, F.-D. Jia, H.-Y. Zhang, J. Mei, W.-C. Liang, F. Zhou, Y.-H. Yu, Y. Liu, J. Zhang, F. Xie, and Z.-P. Zhong, Chin. Phys. B **31**, 090703 (2022).
28. J. Yuan, T. Jin, L. Wang, L. Xiao, and S. Jia, Laser Phys. Lett. **19**, 125207 (2022).
29. D. Anderson, R. Sapiro, L. Gonçalves, R. Cardman, and G. Raithel, Phys. Rev. Appl. **17**, 044020 (2022).
30. Y. Cai, S. Shi, Y. Zhou, Y. Li, J. Yu, W. Li, and L. Li, Phys. Rev. Appl. **19**, 044079 (2023).
31. M. T. Simons, A. H. Haddab, J. A. Gordon, and C. L. Holloway, Appl. Phys. Lett. **114**, 114101 (2019).
32. A. K. Robinson, N. Prajapati, D. Senic, M. T. Simons, and C. L. Holloway, Appl. Phys. Lett. **118**, 114001 (2021).
33. Y. Jiao, L. Hao, X. Han, S. Bai, G. Raithel, J. Zhao, and S. Jia, Phys. Rev. Appl. **8**, 014028 (2017).
34. H. Fan, S. Kumar, J. Sheng, J. P. Shaffer, C. L. Holloway, and J. A. Gordon, Phys. Rev. Appl. **4**, 044015 (2015).
35. D. Adamy, *EW 101: A First Course in Electronic Warfare*, Vol. 101 (Artech House, 2001).
36. F. Jia, H. Zhang, X. Liu, J. Mei, Y. Yu, Z. Lin, H. Dong, Y. Liu, J. Zhang, F. Xie, and Z. Zhong, J. Phys. B: At., Mol. Opt. Phys. **54**, 165501 (2021).
37. K. Dixon, K. Nickerson, D. W. Booth, and J. P. Shaffer, "Rydberg atom-based electrometry using a self-heterodyne frequency comb readout and preparation scheme," arXiv, arXiv:2209.02583 (2022).